In-depth validation of unresolved CFD-DEM simulations of liquid fluidized beds

Victor O. Ferreira[a], Toni El Geitani[c], Daniel Silva Junior[b], Bruno Blais[c], Gabriela C. Lopes[a,b,*]

[a] *Chemical Engineering Graduate Program, Federal University of So Carlos, Rod. Washington Luiz, Km 235 - SP 310, So Carlos, SP 13565-905, Brazil*
[b] *Chemical Engineering Department, Federal University of So Carlos, Rod. Washington Luiz, Km 235 - SP 310, So Carlos, SP 13565-905, Brazil*
[c] *Research Unit for Industrial Flows Processes (URPEI), Department of Chemical Engineering, cole Polytechique de Montral, PO Box 6079, Stn Centre-Ville, Montral, QC, Canada, H3C 3A7*

Abstract

In this work, we assess the accuracy of the unresolved CFD-DEM method by confronting simulated and experimental results of a pilot-scale cylindrical liquid-solid fluidized bed. We used two types of particles with significantly different densities (1029 and 3586 $\mathrm{kg\,m^{-3}}$), allowing for testing a wide range of flow regimes. Comparisons between experimental and simulated particles' dynamics show that the Saffman lift force is essential in predicting the physical dispersion of particles, preventing unphysical plumes. Simulations precisely reproduced the overall force balance in the system. The bed expansion as a function of the inlet velocity results show excellent agreement between simulations and experiments. High agreement between experiments and simulations is observed for the drag models proposed by Di Felice, Rong, and Beetstra but not for Gidaspow. The results validate the use of unresolved CFD-DEM to simulate the liquid-solid fluidized bed.

Keywords: Liquid-solid fluidized bed (LSFB), Unresolved CFD-DEM, FEM-DEM, Multiphase flow.

1. Introduction

Liquid-solids fluidized beds (LSFB) are applied in a wide range of unit operations, including heterogeneous reactions, crystallization, and classification [1]. Its advantages compared to fixed beds include the agitation of particles and the possibility of increasing operational flow rates (way above the minimum fluidization velocity) at a constant pressure drop. Together, the agitation of

*Corresponding author
Email address: gclopes@ufscar.br (Gabriela C. Lopes)

particles and high flow rates increase the heat and/or mass transfer between phases, implying, for example, better temperature control and higher conversion. Additionally, LSFB tend to form well-dispersed beds, which, together with the high degree of agitation, preserve the uniformity of products.

The design of LSFB relies mainly on empirical correlations with little or no phenomenological background. For example, one popular correlation in the design of LSFB is the Richardson-Zaki equation (R-Z) [2]:

$$\frac{U}{U_0} = \bar{\varepsilon}_f^n \tag{1}$$

where U is the fluid inlet velocity, U_0 is the free settling terminal velocity of the particles, $\bar{\varepsilon}_f$ is the fluid (void) fraction in the bed of particles, and n is an empirical parameter of the equation [2]. The R-Z equation predicts the global porosity of the bed, given the characteristics of both flow and particles. However, the precision of predictions is closely dependent on n and U_0, determined by correlations in the literature (e.g., 3, 4, 5) or experimental efforts, both limited to a given range of application. Additionally, the correlation does not predict bed dispersion, preferential path generation, or other localized phenomena. This lack of predictability restricts the applicability of LSFB.

In this sense, Computational Fluid Dynamics (CFD) plays an essential role in understanding such particle-fluid flows. The Volume-Averaged Navier-Stokes (VANS) equations [6] can be numerically solved to provide detailed descriptions of multiphase flows. Authors such as Gidaspow [7] used this concept to model both solid and fluid phases as continuums. This technique is called the Two-Fluid Model (TFM) and has been applied by many authors since then (e.g., 8, 9, 10, 11, 12). The main disadvantage of this technique is that the solid phase is modeled as a continuous phase, in which all particles' movement and interactions are represented by spatial averages. Consequently, it does not evaluate particles' individual behavior.

Alternatively, the unresolved coupling between CFD and the Discrete Elements Method (CFD-DEM) [13, 14, 15] describes the solid phase with significantly more details. This is because the DEM [16, 17] models the motion of the solid phase at the scale of individual particles. This means that each particle has its own movement described by Newton's second law, individually accounting for the collisional, non-collisional (such as gravity), and other forces. In the unresolved CFD-DEM coupling, the mesh elements are larger than particles (preferably three to four times the size of particles) [18], and the fluid properties are described as volume averages within averaging volume (generally mesh elements). The use of volume-averaged properties to describe the fluid and its coupling with a very detailed description of the particle dynamics is key to obtaining accurate results at a reasonable computational cost.

Several authors applied unresolved CFD-DEM [19, 20, 14, 21, 22, 23, 24, 25, 26] to simulate different particle-liquid systems. These studies present promising results, showing that the technique has great potential for these systems. For example, Di Renzo and Di Maio [19] report realistic homogeneity in glass

beads fluidized by water simulation using unresolved CFD-DEM. They also obtained good agreement between the fluid velocity and estimation of the velocity propagation for the transient bed expansion.

One significant challenge is the choice of models for the solid-fluid interaction. In the unresolved CFD-DEM approach, we use correlations to represent drag, lift, (Basset) history, and virtual mass forces. The accuracy of the simulations depends on the accuracy of these correlations. Nijssen et al. [24] showed that forces other than drag can have a non-negligible impact on particles' dynamics of a liquid-solid fluidized bed simulated using unresolved CFD-DEM. In their case, the solids mixing was 20% slower due to the damping caused by the dissipation forces. Nevertheless, the lack of experimental techniques with enough resolution to accurately measure each force separately reduces the reliability of such correlations. That is an important reason why works using VANS frequently neglect forces other than drag. Another reason for the simplification is that most works using unresolved CFD-DEM involve gas-solid systems. In these systems, drag generally dominates other forces. Nonetheless, for liquid-solid systems, this assumption is debatable [27, 24].

Although significant results have been reported for solid-liquid systems, only a few liquid-solid fluidized bed studies comparing experiments and unresolved CFD-DEM simulations are found in the literature [28, 26]. The present research aims to validate the unresolved CFD-DEM method on the simulation of LSFB using FEM. To do so, we confront simulation results with experiments of a pilot-scale cylindrical liquid-solid fluidized bed. The experiments were carried out for alginate and alumina particles, chosen because of their density difference (1029 and 3586 $\mathrm{kg\,m^{-3}}$, respectively), which allowed for the study of a wide range of fluidization regimes. First, we discuss the importance of the Saffman lift force and the smoothing of the void fraction field on the dispersion of particles and flow pattern. After this, we investigate how different mesh topologies may affect this result. Then, we assess the accuracy of the simulation predictions through pressure drop and bed expansion results. Finally, we vary drag force correlations and compare them to experimental results to assess the impact of each aspect on the accuracy of the simulations.

2. CFD-DEM Formulation

The present section briefly describes the equations used within the unresolved CFD-DEM model. For a more detailed description, the authors refer the reader to Zhou et al. [13], Bérard et al. [15], and Gidaspow [7] for the VANS equations, and to Zhu et al. [16], Blais et al. [29], and Golshan et al. [17] for the DEM modeling.

The simulations were carried out using Lethe [30, 17, 31], an open-source CFD and DEM software with resolved and unresolved CFD-DEM coupling capabilities. We refer the reader to Geitani et al. [31, 32] for further details about the numerical strategies, including derivation of the weak form of VANS equations, stabilization strategies, and void fraction smoothing.

2.1. Solid phase modeling

In the DEM approach, we apply Newtons second law of motion on each moving particle to calculate both its linear and tangential momentum, respectively represented by Equations 2 and 3:

$$m_i \frac{d\boldsymbol{v}_i}{dt} = \sum_{j=1,j\neq i}^{N_p} (\boldsymbol{f}_{c,ij}) + \sum_{j,j\neq i}^{N_p} (\boldsymbol{f}_{nc,ij}) + \boldsymbol{f}_{pf,i} + \boldsymbol{f}_{g,i} \tag{2}$$

$$I_i \frac{d\boldsymbol{\omega}_i}{dt} = \sum_{j,j\neq i}^{N_p} (\boldsymbol{M}_{t,ij} + \boldsymbol{M}_{r,ij}) \tag{3}$$

where the subscripts i refer to the i^{th} particle interacting with the j^{ith} particle, N_p is the number of particles, $\boldsymbol{v}$ represents the velocity of the particle, $\boldsymbol{f}_c$ the contact forces, $\boldsymbol{f}_{nc}$ the non-contact forces, $\boldsymbol{f}_g$ the gravity force and $\boldsymbol{f}_{pf}$ the sum of forces exerted over particles by the fluid phase, while $\boldsymbol{M}_t$ and $\boldsymbol{M}_r$ are the tangential and rolling friction torques. In this work, the non-contact forces are neglected due to their small magnitude compared with the contact and coupling forces.

We modeled the collisions using the soft-sphere collision model proposed by Cundall and Strack [33]. In Equation (2), the contact forces can be decomposed in normal ($\boldsymbol{f}_{cn,ij}$) and tangential ($\boldsymbol{f}_{ct,ij}$) contact forces, such that:

$$\boldsymbol{f}_{c,ij} = \boldsymbol{f}_{cn,ij} + \boldsymbol{f}_{ct,ij} = -k_{n,ij}\boldsymbol{\delta}_{n,ij} - \gamma_{t,ij}\dot{\boldsymbol{\delta}}_{n,ij} - k_{t,ij}\boldsymbol{\delta}_{t,ij} - \gamma_{t,ij}\dot{\boldsymbol{\delta}}_{t,ij} \tag{4}$$

in which the subscript n and t refer to normal and tangential directions, respectively. The overlap ($\boldsymbol{\delta}$) and its derivative with respect to time ($\dot{\boldsymbol{\delta}}$) are both used to calculate the contact forces. In Equation (4), the tangential overlap ($\boldsymbol{\delta}_{t,ij}$) is limited by Coulomb's law, written as:

$$\boldsymbol{\delta}_{t,ij} \leq -\mu_{s,ij} \left|\boldsymbol{f}_{cn,ij}\right| \frac{\boldsymbol{\delta_{n,ij}}}{\left|\boldsymbol{\delta_{n,ij}}\right|} \tag{5}$$

For both normal and tangential directions, k and γ are the stiffness and the damping coefficients of the colliding pair, calculated based on the mechanical properties of the particles, which are the effective Young's Modulus (Y), the coefficient of restitution (e) and Poisson ratio (ν). Table 1 summarizes the Equations for stiffness and damping calculation.

Using $\boldsymbol{f}_{cn,ij}$ and $\boldsymbol{f}_{ct,ij}$, the tangential and rolling friction torques ($\boldsymbol{M}_{t,ij}$ and $\boldsymbol{M}_{r,ij}$, respectively) can be calculated by:

$$\boldsymbol{M}_{t,ij} = \boldsymbol{r}_i \times (\boldsymbol{f}_{ct,ij}) \tag{6}$$

$$\boldsymbol{M}_{r,ij} = -\mu_{r,ij} \left|\boldsymbol{f}_{ct,ij}\right| \frac{\boldsymbol{\omega}_{ij}}{\left|\boldsymbol{\omega}_{ij}\right|} R^*_{ij} \tag{7}$$

Table 1: DEM equations

Property	**Equation**
Radius of particle i	R_i
Distance between i and contact point	$\boldsymbol{r}_i$
Equivalent mass	$\frac{1}{m^*_{ij}} = \frac{1}{m_i} + \frac{1}{m_j}$
Equivalent radius	$\frac{1}{R^*_{ij}} = \frac{1}{R_i} + \frac{1}{R_j}$
Equivalent Young's modulus	$\frac{1}{Y^*_{ij}} = \frac{1-\nu_i^2}{Y_i} + \frac{1-\nu_j^2}{Y_j}$
Equivalent shear modulus	$\frac{1}{G^*_{ij}} = \frac{2(2+\nu_i^2)(1-\nu_i^2)}{G_i} + \frac{2(2+\nu_j^2)(1-\nu_j^2)}{G_j}$
Normal stiffness	$k_{n,ij} = \frac{4}{3} Y^*_{ij} \sqrt{R^*_{ij} \boldsymbol{\delta_{n,ij}}}$
Tangential stiffness	$k_{t,ij} = 8 G^*_{ij} \sqrt{R^*_{ij} \boldsymbol{\delta_{n,ij}}}$
Normal damping	$\gamma_{n,ij} = -2\sqrt{\frac{5}{6}} \frac{ln(e)}{\sqrt{ln^2(e)+\pi^2)}} \sqrt{\frac{2}{3} k_{n,ij} m^*_{ij}}$
Tangential damping	$\gamma_{t,ij} = -2\sqrt{\frac{5}{6}} \frac{ln(e)}{\sqrt{ln^2(e)+\pi^2)}} \sqrt{k_{t,ij} m^*_{ij}}$

where the coefficient of rolling friction ($\mu_{r,ij}$) and the equivalent radius (R^*_{ij}) are calculated by the Equations in Table 1.

In this work, we consider large particles ($d_p > 1\,\text{mm}$), and we can neglect the non-contact forces $\boldsymbol{f}_{nc,ij}$ since they are small compared to the contact $\boldsymbol{f}_{c,ij}$ and particle-fluid forces $\boldsymbol{f}_{pf,i}$. The source of the latter is the interaction between the liquid and the solid particles, which is calculated by:

$$\boldsymbol{f}_{pf,i} = \boldsymbol{f}_{d,i} + \boldsymbol{f}_{\nabla p,i} + \boldsymbol{f}_{\nabla \cdot \boldsymbol{\tau},i} + \boldsymbol{f}_{Ar,i} + \boldsymbol{f}''_i \tag{8}$$

for particle i, where $\boldsymbol{f}_{d,i}$ represents the drag, $\boldsymbol{f}_{\nabla p,i}$ is the force due to the pressure gradient, $\boldsymbol{f}_{\nabla \cdot \boldsymbol{\tau},i}$ is the force due to the shear stress with the fluid, and $\boldsymbol{f}''_i$ stands for the rest of forces less frequently considered due to their magnitude, represented by:

$$\boldsymbol{f}''_i = \boldsymbol{f}_{\text{vm},i} + \boldsymbol{f}_{\text{B},i} + \boldsymbol{f}_{\text{Mag},i} + \boldsymbol{f}_{\text{Saff},i} \tag{9}$$

where the terms of $\boldsymbol{f}''_i$ represent virtual mass, Saffman lift, Magnus lift, and the Basset forces, respectively. In the present work, we evaluated the influence of the Saffman lift force in the LSFB. Magnus lift, Basset, and virtual mass forces were also neglected due to the same assumptions used by Di Renzo and Di Maio [19], namely that it is not possible to extrapolate the expression for these forces, which were mathematically derived assuming very dilute systems, to a highly concentrated contact-driven system. The remaining terms of Eq. 8 are described in Section 2.3.

2.2. Liquid phase modeling

The equations for fluid-particle systems were first developed considering the two-fluid model, which assumes two continuous phases. The idea is that each phase has a fraction of the cell properties proportional to the volume it occupies. In this sense, the Navier-Stokes equations represent not only the fluid phase

but a volume average of the mixture. The Volume-Averaged Navier-Stokes Equations are used in TFM and unresolved CFD-DEM to represent the fluid phase.

The VANS equations can be expressed in two forms as described by Zhou et al. [13], referred to as model A and B (Sets II and I, respectively), to represent the fluid phase. In both forms, the continuity equation for an incompressible flow is written as:

$$\frac{\partial \varepsilon_f}{\partial t} + \nabla \cdot (\varepsilon_f \boldsymbol{u}) = 0 \tag{10}$$

where $\boldsymbol{u}$ is the fluid velocity vector, and ε_f is the void (fluid volume) fraction, calculated by:

$$\varepsilon_f = 1 - \frac{\sum_i^{N_{p,C}} V_{p,i}}{\Delta V_{\Omega_C}} = 1 - \varepsilon_p \tag{11}$$

where $N_{p,C}$ is the number of particles inside the cell Ω_C with volume ΔV_{Ω_C}

The difference between models A and B comes from the way we represent pressure and shear stress. In model A, both terms are assumed to be in both fluid and solid phases, which makes the momentum equation takes the form of:

$$\rho_f \left[\frac{\partial \varepsilon_f \boldsymbol{u}}{\partial t} + \nabla \cdot (\varepsilon_f \boldsymbol{u} \otimes \boldsymbol{u}) \right] = -\varepsilon_f \nabla p + \varepsilon_f \nabla \cdot \boldsymbol{\tau} - \boldsymbol{F}_{pf}^A \tag{12}$$

where $\boldsymbol{\tau}$ is the viscous shear stress tensor, and $\boldsymbol{F}_{pf}^A$ is the fluid-particle momentum exchange (source) term for model A:

$$\boldsymbol{F}_{pf}^A = \frac{1}{\Delta V_{\Omega_C}} \sum_i^{N_{p,C}} (\boldsymbol{f}_{d,i} + \boldsymbol{f}_i'') = \frac{1}{\Delta V_{\Omega_C}} \sum_i^{N_{p,c}} (\boldsymbol{f}_{pf,i} - \boldsymbol{f}_{\nabla p} - \boldsymbol{f}_{\nabla \cdot \boldsymbol{\tau}} - \boldsymbol{f}_{Ar}) \tag{13}$$

where the index $N_{p,C}$ stands for the number of particles inside the cell Ω_C in which the averaging is applied. On the other hand, in model B, the pressure and shear stress are entirely in the fluid phase. This way, we can write the momentum equation for model B as:

$$\rho_f \left[\frac{\partial \varepsilon_f \boldsymbol{u}}{\partial t} + \nabla \cdot (\varepsilon_f \boldsymbol{u} \otimes \boldsymbol{u}) \right] = -\nabla p + \nabla \cdot \boldsymbol{\tau} - \boldsymbol{F}_{pf}^B \tag{14}$$

where $\boldsymbol{F}_{pf}^B$ is the interaction term for model B, written as:

$$\boldsymbol{F}_{pf}^B = \frac{1}{\Delta V_{\Omega_C}} \sum_i^{N_{p,c}} \boldsymbol{f}_{pf,i} + \boldsymbol{f}_i'' \tag{15}$$

The shear stress tensor is expressed as:

$$\boldsymbol{\tau} = \mu \left[(\nabla \cdot \boldsymbol{u}) + (\nabla \cdot \boldsymbol{u})^T - \frac{2}{3} (\nabla \cdot \boldsymbol{u} \boldsymbol{I}) \right] \tag{16}$$

where μ is the dynamic viscosity and $\boldsymbol{I}$ is the identity matrix.

2.3. Interphase momentum transfer modeling

The interphase momentum coupling between numerical solutions for the two phases is done through the interphase momentum exchange term $\boldsymbol{F}_{pf}$. The components of this term are represented in what follows.

2.3.1. Pressure and buoyancy forces

Pressure and buoyancy (or Archimedes) forces are treated separately in the present work. As explained in Section 2.2, in Lethe the fluid pressure gradient ∇p does not account for the hydrostatic pressure. This means that the force due to the pressure gradient takes into account only the undisturbed pressure. As a consequence, the buoyancy force needs to be explicitly applied in Eq. (8). The expressions that represent the pressure gradient and buoyancy forces are, respectively:

$$\boldsymbol{f}_{\nabla p,i} = V_{p,i} \nabla p \tag{17}$$

$$\boldsymbol{f}_{Ar,i} = V_{p,i} \rho_f \boldsymbol{g} \tag{18}$$

where $V_{p,i}$ is the volume of the particle i, ρ_f is the density of the fluid, p stands for dynamic pressure, $\boldsymbol{g}$ is the gravity acceleration vector.

2.3.2. Shear force

The force due to the fluid viscous shear stress is:

$$\boldsymbol{f}_{\nabla \cdot \boldsymbol{\tau},i} = V_{p,i} \boldsymbol{\nabla} \cdot \boldsymbol{\tau} \tag{19}$$

2.3.3. Drag force

Drag stands for the friction between a body and the surrounding fluid. In fluidization, drag and buoyancy counterbalance gravity, lifting and holding particles up in the fluidized state. Drag is defined as:

$$\boldsymbol{F}_d = \sum_{i}^{N_{p,C}} \boldsymbol{f}_{d,i} = \sum_{i}^{N_{p,C}} \beta_i \left(\boldsymbol{u} - \boldsymbol{v}_i \right) \tag{20}$$

In unresolved CFD-DEM, since the fluid is described at a mesoscale, drag is conveniently defined as a function of a coefficient β_i, usually referred to as the "interphase momentum transfer coefficient". However, this is only true for model A because, in the absence of $\boldsymbol{f}_i''$, $\boldsymbol{F}_{pf}^A = \boldsymbol{F}_d$ (see Eq. (13)).

Several authors tried to determine β_i for particle-fluid systems. Gidaspow [7] developed a correlation based on Ergun [34] and Wen and Yu [35] equations for the pressure drop in particle-fluid flows. Considering perfectly spherical particles:

$$\beta_i = \begin{cases} 150 \frac{(1-\varepsilon_f)^2 \mu}{(\varepsilon_f d_p)^2} + 1.75 \frac{\rho_f |\boldsymbol{u} - \boldsymbol{v}_i| (1-\varepsilon_f)}{d_p \varepsilon_f}, \text{ for } \varepsilon_f < 0.8 \\ \frac{3}{4} C_{D,i} \frac{\rho_f (1-\varepsilon_f) |\boldsymbol{u} - \boldsymbol{v}_i|}{d_p}, \text{ for } \varepsilon_f \geq 0.8 \end{cases} \tag{21}$$

where $C_{D,i}$ is the drag coefficient for a single particle, calculated by:

$$C_{D,i} = \begin{cases} \frac{24}{\mathrm{Re}_{p,i}} \left(1 + 0.15\mathrm{Re}_{p,i}^{0.687}\right), \text{ for } \mathrm{Re}_{p,i} < 1000 \\ C_{D,i} = 0.44, \text{ for } \mathrm{Re}_{p,i} \geq 1000 \end{cases} \tag{22}$$

where the Reynolds number of the particles $\mathrm{Re}_{p,i}$ is:

$$\mathrm{Re}_{p,i} = \varepsilon_f \rho_f \left|\boldsymbol{u} - \boldsymbol{v}_i\right| d_p / \mu \tag{23}$$

Following a similar approach, other authors proposed correlations for β_i mainly finding a function $G(\varepsilon_f)$ that represents the ratio between the drag coefficient $C_{D,i}$ and drag coefficient for a single isolated particle C_{D0}:

$$\frac{C_{D,i}}{C_{D0}} = G(\varepsilon_f, \mathrm{Re}_{p,i}) \tag{24}$$

In this approach, β_i is:

$$\beta_i = \frac{1}{2} C_{D0} \frac{\pi d_p^2}{4} \rho_f \left|\boldsymbol{u} - \boldsymbol{v}_i\right| G(\varepsilon_f, \mathrm{Re}_{p,i}) \tag{25}$$

Di Felice [36] and Rong et al. [37] proposed a correlations for $G(\varepsilon_f, \mathrm{Re}_{p,i})$ based on C_{D0} proposed by DallaValle [38]:

$$C_{D0} = \left(0.63 + \frac{4.8}{\sqrt{\mathrm{Re}_p}}\right)^2 \tag{26}$$

The correlation proposed by Di Felice for $G(\varepsilon_f, \mathrm{Re}_{p,i})$ is:

$$G(\varepsilon_f, \mathrm{Re}_{p,i}) = \varepsilon_f^{2-\left\{3.7-0.65exp\left[-\frac{(1.5-log_{10}\mathrm{Re}_{p,i})^2}{2}\right]\right\}} \tag{27}$$

This equation assumes the strong hypothesis that the exponent is a function only of Re_p and not of ε_f. As shown by several authors [39, 40, 41, 42, 37], this hypothesis leads to errors in the estimation of drag. The Rong correlation is similar to Di Felice but tries to account for the effect of the void fraction on the exponent, written as:

$$G(\varepsilon_f, \mathrm{Re}_{p,i}) = \varepsilon_f^{2-\left\{2.65(\varepsilon_f+1)-(5.3-3.5\varepsilon_f)\varepsilon_f^2 exp\left[-\frac{(1.5-log_{10}\mathrm{Re}_{p,i})^2}{2}\right]\right\}} \tag{28}$$

An alternative approach was used by Beetstra et al. [41]. It determines a normalized drag force $F(\varepsilon_f, \mathrm{Re}_{p,i})$ by correcting the drag force using the Stokes-Einstein drag ($3\pi d_p \boldsymbol{u}$), the latter representing the drag experienced by a single isolated particle ($\varepsilon_f \to 1$) in the limit of $\mathrm{Re}_{p,i} \to 0$:

$$F(\varepsilon_f, \mathrm{Re}_{p,i}) = \frac{\boldsymbol{F}_d}{3\pi d_p (\boldsymbol{u} - \boldsymbol{v}_i)} \tag{29}$$

The authors proposed correlations for both mono and poly-dispersed beds. The correlation for mono-dispersed flows is:

$$F(\varepsilon_f, \mathrm{Re}_{p,i}) = \frac{10\,(1-\varepsilon_f)}{\varepsilon_f^2} + \varepsilon^2\left(1 + 1.5\varepsilon_f^{0.5}\right) + \frac{0.413\mathrm{Re}_{p,i}}{24\varepsilon_f^2}\left[\frac{(1/\varepsilon_f) + 3\varepsilon_f\,(1-\varepsilon_f) + 8.4\mathrm{Re}_{p,i}^{-0.343}}{1 + 10^{3(1-\varepsilon_f)}\mathrm{Re}_{p,i}^{-(1+4(1-\varepsilon_f))/2}}\right] \tag{30}$$

2.3.4. Saffman lift force

The lift force can be separated into two components, usually referred to as Saffman and Magnus. Both forces act perpendicular to the relative velocity between phases, but the first happens due to the gradient of the fluid velocity field along the particle, and the latter is caused by the particles' rotation [43]. Since the rotation of the particles is dissipated by the presence of water and collisions in the LSFB, the Magnus force was neglected in the present work.

The Saffman component of the lift forces acting over a particle i can be represented by combining the correlation proposed by Saffman [44, 45] and the lift coefficient proposed by Mei [46], usually referred to as Saffman-Mei lift force model, and is calculated by:

$$\boldsymbol{f}_{\mathrm{Saff},i} = 1.161 C_{\mathrm{Saff},i} d_p^2 (\mu\rho_f)^{1/2} \left|\boldsymbol{\omega}_{c,i}\right|^{-1/2} \left[(\boldsymbol{u} - \boldsymbol{v}_i) \times \boldsymbol{\omega}_{c,i}\right] \tag{31}$$

where the vorticity $\boldsymbol{\omega}_{c,i}$ corresponds to the curl of the vector field, calculated as:

$$\boldsymbol{\omega}_{c,i} = \nabla \times \boldsymbol{u} \tag{32}$$

In equation (31), $C_{\mathrm{Saff},i}$ is the Saffman lift coefficient, calculated by:

$$C_{\mathrm{Saff},i} = \begin{cases} \left(1 - 0.3314\alpha^{1/2}\right)\exp\left(\frac{-\mathrm{Re}_{p,i}}{10}\right) + 0.3314\alpha^{1/2}, \text{ for } \mathrm{Re}_{p,i} \leq 40 \\ 0.0524(\alpha_l \mathrm{Re}_{p,i})^{1/2}, \text{ for } \mathrm{Re}_{p,i} > 40 \end{cases} \tag{33}$$

where α is:

$$\alpha = \frac{d_p}{2\left|\boldsymbol{u} - \boldsymbol{v}_i\right|}\left|\boldsymbol{\omega}_{c,i}\right| \tag{34}$$

3. Fluidized Bed Experiment

In the present section, we describe the materials and experimental setup used in the validation campaign.

3.1. Particles

We used two groups of particles in this work: alginate and alumina. The alumina particles were used as received. We synthesized the alginate particles by dropping a 20 $\mathrm{g\,L^{-1}}$ sodium alginate solution (Fisher Chemical) impregnated with titanium dioxide powder (mass ratio 25:2) into a 15 $\mathrm{g\,L^{-1}}$ barium chloride

solution. The sodium alginate gelifies when in contact with the barium chloride, forming barium alginate particles. We added titanium dioxide powder to increase the weight of the particles, making them heavier than water. We refer the reader to works by Lopes et al. [47] and Melo et al. [48] for more reference on manufacturing these particles.

We characterized both groups of particles in density, diameter, and terminal settling velocity. The diameter of the particles was measured by capturing images with 20 random samples and processing the images using the image processing library called OpenCV [49]. The software was calibrated using Acrylonitrile Butadiene Styrene (ABS) commercial particles ($d_p = 5.95 \pm 0.01$ mm) as reference. We maintained the distance between the camera and the particles for all samples. In this work, we considered the diameter of all particles equivalent to the superficial diameter of the set of 20 samples.

To measure the particles' apparent densities, we applied the pycnometry method using a 25 mL pycnometer and distilled water as reference fluid. Since the alginate particles present a high water content and alumina is a porous material, we measured their densities after soaking them in water for at least 24 hours.

For the terminal settling velocity, we tracked the falling trajectory of ten particles inside a 20 cm wide 1 m height square-based tank using a high-speed camera (correlation DSC-RX100 M, brand Sony) at 960 frames per second. We used the open-source image processing software Tracker [50] to measure their velocities.

The particles' samples were weighed before every fluidization experiment. For all experiments with alginate, the total weight of the particles was 1.1 kg, and for the alumina, 4.0 kg.

The characterization results are presented in Table 2.

Table 2: Summary of particles' characterization results.

Characteristic	**Alginate**	**Alumina**
Total mass (M_p)	1.1 kg	4.0 kg
Density (ρ_p)	1029 ± 1 kg m^{-3}	3586 ± 10 kg m^{-3}
Diameter (d_p)	2.66 ± 0.10 mm	3.09 ± 0.16 mm
Terminal settling velocity (U_0)	3.03 ± 0.01 cm s^{-1}	48.02 ± 0.02 cm s^{-1}

3.2. Fluidization experiments

We used water as the fluid in all fluidization experiments. The experimental setup consists of a 1 m height, 10 cm diameter cylindrical fluidized bed column. A schematic representation of the experimental setup is presented in Figure 1a.

We used Arduino-based sensors in all experimental measurements. Since we conducted the experiments using two different ranges of inlet flow rates, we applied different Hall effect flow rate sensors according to the particles: for the experiments with alginate particles, we used the YF-S201 (1 30 L min^{-1}); while for the alumina we used the YF-G1 (2 100 L min^{-1}). The Arduino system

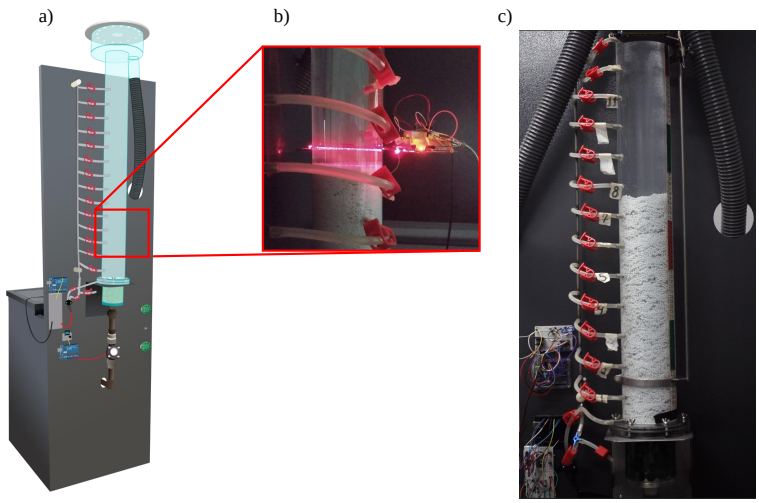

Figure 1: Schematic representation of a) the equipment and b) the laser apparatus used for bed height measurement.

registered the instantaneous inlet flow rate and calculated the time average during the experiments. The inlet conditions of the experiments are described in Table 3.

Table 3: Summary of fluidization experiments inlet conditions.

Fluid inlet condition	**Alginate**	**Alumina**
Number of inlet flow rates	7	8
Flow rate range	2 - 5 $\mathrm{L\,min^{-1}}$	40 - 75 $\mathrm{L\,min^{-1}}$
Inlet Reynolds number range	498 - 1244	9954 - 18664
Range of U/U_0	0.14 - 0.35	0.18 - 0.33

We used an analogic Negative Temperature Coefficient (NTC) thermistor to monitor the water temperature. The average temperature among the experiments was 30 °C. We used this value to estimate the water's density and viscosity in the simulations.

3.2.1. Pressure drop

In the fluidization regime, the total pressure drop along the bed height, $-\Delta p$ is constant, regardless of the inlet flow rate [5]. It can be calculated using the following equation:

$$-\Delta p = \frac{M_p \left(\rho_p - \rho_f\right) g}{\rho_p A_b} \tag{35}$$

where M_p is the total mass of the particles inside the bed and A_b is the cross-section area of the equipment. The total pressure drop for the alginate particles is 41.64 Pa, and for the alumina, it is 3608.55 Pa.

3.2.2. Bed porosity

The fluidized bed porosity $\bar{\varepsilon}_f$ is a convenient way of representing the bed expansion since it is dimensionless, and both quantities have a direct relation. To determine the experimental bed expansion, we measure the bed porosity using two techniques, depending on the particles' characteristics.

For the alginate particle, we measure the porosity using a direct measurement of the bed height since the top of the bed is calm and flat. We used a laser apparatus comprising a semi-circular platform holding a 5 V laser diode, a Light Dependent Resistor light sensor (LDR), and an Arduino microcontroller. The platform is free to move along the equipment's height and keeps the laser beam pointing to the LDR. The microcontroller registers the signal returned by the LDR and calculates the moving average of this value at 15-second intervals. Figure 1b shows a picture of the laser apparatus.

During the fluidization experiments, we measured the bed height by positioning the laser apparatus at the height where the moving average of the analog signal is within a threshold value $\pm 10\%$ and measured the laser height. The threshold value corresponds to the average between the LDR analog signal measured at a particle-free zone and an utterly interrupted beam.

With the experimental bed height, we calculated $\bar{\varepsilon}_f$ using:

$$\bar{\varepsilon}_f = 1 - \left(\frac{M_p}{\rho_p A_b H_b} \right) \tag{36}$$

Since the alumina particles are heavier and tend to form a more unstable bed top, the laser technique could not be applied. Instead, we measured the bed expansion using the differential pressure profile along the bed height. As shown in Figure 1c, pressure outlets are positioned along the height of the bed, and we measured the differential pressure to each point. With the differential pressure ($-\Delta p$) and the height of each pressure outlet (Δz), we found the slope of the differential pressure curve along the bed height ($-dp/dz$) and calculated the bed porosity using the following relation [5]:

$$\bar{\varepsilon}_f = 1 - \left[\frac{-\mathrm{d}p/\mathrm{d}z}{(\rho_p - \rho_f)g} \right] \tag{37}$$

For comparison reasons, we estimated the bed porosity using R-Z (Equation 1). The index n was calculated using the correlation proposed by [3]. To evaluate the fitting between the estimated and simulated results with respect to the experiments, we apply the root-mean-squared error (RMSE), calculated by:

$$RMSE = \sqrt{\frac{1}{N} \sum_{i}^{N} \left(y'_i - y_{exp,i} \right)^2} \tag{38}$$

where N is the number of inlet conditions (i.e., 7 for the alginate and 8 for the alumina particles), y'_i is the estimated or simulated result, and $y_{exp,i}$ is the experimental result. The RMSE is especially useful for such analysis for

highlighting outliers, which can be helpful in cases where the results are close to each other.

4. Simulation Setup

The simulations were carried out on Lethe [30, 17, 31, 32], a Finite Elements Method (FEM) open-source software with CFD, DEM, and CFD-DEM coupling capabilities. We used the setup described in Table 4 as a benchmark for all simulations. Unless mentioned, the parameters are the same for all simulations.

Table 4: Simulation parameters.

Parameter	**Alginate**	**Alumina**
Total real-time	35 s	20 s
Time integration method	BDF1	BDF1
CFD time-step and coupling interval (Δt_{CFD})	0.001 s	0.001 s
DEM time-step (Δt_{DEM})	0.000 01 s	0.000 01 s
Output time-step (Δt_{DEM})	0.25 s	0.10 s
Diameter of the cylinder (D_b)	10 cm	10 cm
Height of the cylinder (H_b)	1.10 m	1.10 m
Mesh ($n_r \times n_\theta \times n_z$)	$6 \times 16 \times 132$	$6 \times 16 \times 132$
Liquid density (ρ_f)	$996.78\,\mathrm{kg\,m^{-3}}$	$996.78\,\mathrm{kg\,m^{-3}}$
Liquid dynamic viscosity (μ)	8.352×10^{-4} Pa s	8.352×10^{-4} Pa s
Number of particles (N_p)	107960	72400
Diameter of the particles (d_p)	2.66 mm	3.09 mm
Density of the particles (ρ_p)	$1029\,\mathrm{kg\,m^{-3}}$	$3586\,\mathrm{kg\,m^{-3}}$
Young's modulus (Y)	10 MPa	10 MPa
Coefficient of restitution (e)	0.9	0.9
Poisson ratio (ν)	0.3	0.3
Coefficient of rolling friction (μ_r)	0.2	0.2
Coefficient of sliding friction (μ_f)	0.1	0.1
VANS model type	A	A
Void fraction calculation scheme	PCM	PCM
Void fraction smoothing length	$2.0 \times d_p$	$2.0 \times d_p$
Boundary conditions at the walls	free slip	free slip
Drag model	Rong et al. [37]	Rong et al.[37]
Gravity (g)	$9.81\,\mathrm{m\,s^{-2}}$	$9.81\,\mathrm{m\,s^{-2}}$

The DEM and CFD time steps were selected such that one CFD time step occurred every 100 DEM time steps. The coupling time step was equal to the CFD time step for all simulations. We applied the first-order Backward Differentiation (BDF1) method for the time-stepping. Lethe addresses turbulence implicitly by applying an implicit Large Eddy Simulation (LES) approach, demonstrating high accuracy in describing turbulent systems [31, 51].

Apart from the number of particles (N_p), density (ρ_p), and diameter(d_p), we used the same DEM parameters for both alumina and alginate particles. The

collisional properties, such as Young's modulus and coefficient of restitution, were kept the same for both walls and particles.

Figure 2 is a schematic representation of the mesh and initial packing used in the simulations. Details about the mesh refinement are provided in Table 4.

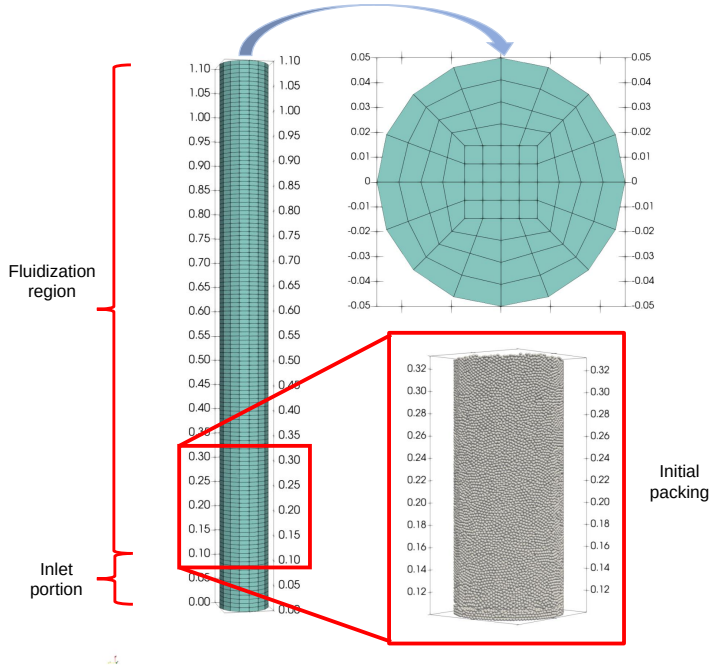

Figure 2: Schematic representation of the mesh and initial packing of particles (units in meters).

As presented in Figure 2, the inlet portion corresponds to a 10 cm height flow calming region. This region without particles helps stabilize the flow below the bed of particles.

The precise calculation of the void fraction is key to obtaining good simulation results. To achieve such precision, the ratio between the size of cells and particles should be high enough so that the void fraction values are representative. One popular way to represent this ratio is using the ratio between the characteristic length of the cells (S_c) and the diameter of the particles. The characteristic length of the cells is calculated based on the cells' volume (V_c) as:

$$S_c = V_c^{1/3} \tag{39}$$

Since the domain is cylindrical, the mesh elements are not all of the same sizes. This implies a variation in S_c/d_p within the domain. Figure 3 shows the distribution of S_c/d_p with the cross-section of the domain for both particles.

We applied the PCM void fraction scheme for the void fraction calculation.

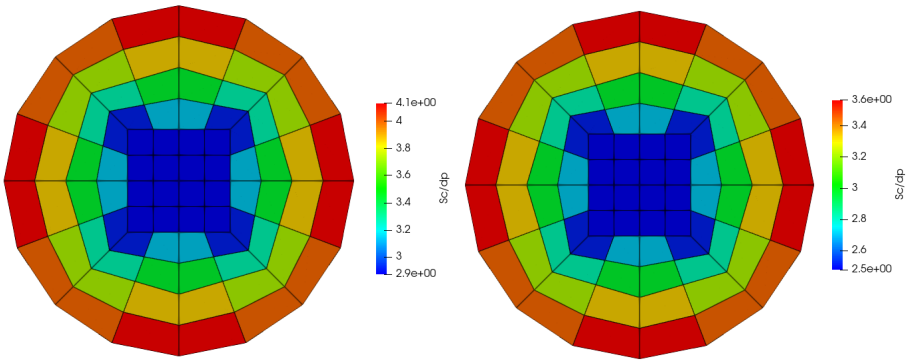

(a) Alginate (b) Alumina

Figure 3: S_c/d_p for (a) alginate and (b) alumina particles.

To avoid sharp discontinuities and enhance numerical stability, we smoothed the void fraction for a length 2 times the diameter of the particles. This is done by adding $\int_\Omega L^2 \nabla\varphi_i \nabla\varphi_j d\Omega$ to the left-hand side of the $\mathcal{L}^2$ projection equation for the void fraction, resulting in the following:

$$\int_\Omega \varphi_i \alpha_{f,j} \varphi_j d\Omega + \int_\Omega L^2 \nabla\varphi_i \nabla\varphi_j d\Omega = \int_\Omega \varepsilon_{f,i} \varphi_i d\Omega \tag{40}$$

where α_f is the projected void fraction, L is the smoothing length, Ω is the domain in which the equation is being resolved (CFD cell), and φ is the basis (hat) function. We refer the reader to the article by Geitani et al. [32] for details about the smoothing strategy and its effect on numerical stability.

Initially, all simulations start with the particles completely static and sedimented. The inlet velocity is imposed at t = 0, and after some time, the fluidized bed reaches a pseudo-steady state. To find when the pseudo-steady state is reached, we calculated the instantaneous porosity of the bed at each output time-step. We considered that the pseudo-steady state was reached when the instantaneous porosities stabilizes around the average among the last 5 seconds of the simulation. For the alginate and the alumina particles, it was reached at around 10 and 4 seconds in real-time, respectively. To guarantee that all results were captured in the pseudo-steady state and are not influenced by the initial bed expansion, all the comparisons with the experimental results are made 5 seconds after the moment when the pseudo-steady state was reached. We present the porosity results as a function of the ratio between the fluid inlet velocity and the terminal velocity of the particles (U/U_0) so that the results follow the shape of Equation 1.

5. Results and Discussion

The main objective of the present work is to prove the validity of the unresolved CFD-DEM method on the simulation of the LSFB. To do so, we start with a qualitative analysis of the particle dynamics inside the equipment, and then the quantitative analysis proceeds with the comparison between experimental data and simulations.

In this sense, we first discuss the importance of void fraction smoothing and the Saffman lift force to obtain accurate particle distribution. To do so, we qualitatively compare particles' experimental and simulated behaviors. Then, since we have a restrictive geometry (small equipment to particle size), we discuss the mesh choice. After this, we proceed to the quantitative validation of the simulations, comparing them with experimental results for pressure drop and bed expansion. Finally, we compare different drag correlations to investigate the robustness.

5.1. Flow structures, void fraction, and the importance of the Saffman lift force

For all simulations, we observed critical channeling at the walls. Clear evidence of this channeling is presented in Figure 4, where lines represent the ratio between two fluid velocities: the one at the center of the bed of particles and the spatial average of the velocities close to the walls (both at the same height).

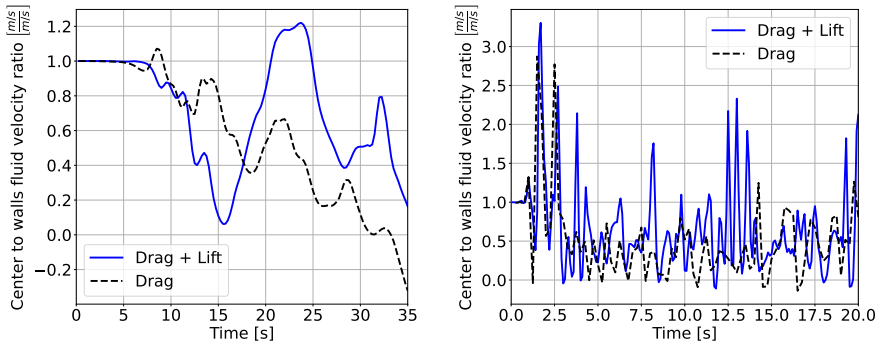

(a) Alginate (b) Alumina

Figure 4: Center to walls velocity ratio for (a) alginate and (b) alumina particles, at $U/U_0 = 0.3595$ and $U/U_0 = 0.3270$, respectively.

As shown in Figure 4, the velocity close to the walls is higher than in the center for almost the entire simulated time. The reason for this relies upon two factors: firstly, the void fraction is naturally higher closer to the walls due to the arrangement of the particles, and secondly, S_c/d_p decreases towards the center of the equipment as shown in Figure 3, virtually distorting the distribution of the void fraction field. The first phenomenon responsible for the void fraction distortion cannot be avoided since it is inherent to the particles' distribution. However, the second effect significantly diminished with void fraction smoothing.

Since the drag correlations are highly dependent on the void fraction, thus, distortion of the void fraction virtually increments drag in regions with smaller cells. As a reaction, the fluid feels a higher resistance in the center of the equipment than the walls, consequently being pushed toward the walls, producing channeling. If no void fraction smoothing strategy is used, the difference between the drag force experienced in the middle of the equipment and close to the walls would be even higher.

In real life, two things reduce this channeling effect: no-slip at the walls and interphase forces in the radial direction. Since the mesoscale of the fluid discretization is not fine enough to represent the boundary layer formed by the fluid friction with the walls, particles are pushed far from the channeling. With nothing to counterbalance this effect, the pseudo-steady state of the bed is unstable. The consequence of this set of phenomena is the unrealistic pluming of particles, easily visible at the top of the bed, as shown in Figures 5 and 6.

This pluming effect is significantly diminished with Saffman lift forces since the channeling is not as persistent. The Saffman lift force pushes the particles towards and away from the channeling regions, which breaks the flow pattern, spreading the fluid and creating a more realistic fluid velocity distribution in the pseudo-steady-state. As a consequence, bed height and uniformity of particle distribution are increased, and the void fraction distortion is compensated. With the more uniform distribution of particles, drag distribution is also more uniform, and the pseudo-steady-state is more stable. Uniformity is a crucial aspect to be taken into account since uniformity is one of the main characteristics of LSFB. These conclusions agree with previous studies by Koreich et al. [10] and Zbib et al. [52]. For this reason, we apply the Saffman lift force in all subsequent simulations in this work.

5.2. Validation of the simulations

The simulations were validated by comparing the pressure drop and the bed porosity with experimental results.

5.2.1. Pressure drop

We compare the simulated total pressure difference with the one calculated by Equation 35 with a 0.95 two-tailed confidence interval ($\alpha = 0.05$). The comparative results are presented in 7. For the simulation results, the error bars correspond to a temporal standard deviation.

For almost all simulations, the total pressure difference was precisely reduced, standing within the 95% confidence interval region, even accounting for the temporal oscillations represented by the standard deviation. This means that the numerical results precisely represent the pressure difference, correctly accounting for the mass of all particles in the force balance.

Few simulated results, mainly the alginate particles, especially at low inlet velocities, did not reach the expected pressure drop. This is caused by the smoothing of the void fraction, which virtually increases the void fraction of cells right above the bottom wall of the equipment. This slight increase in

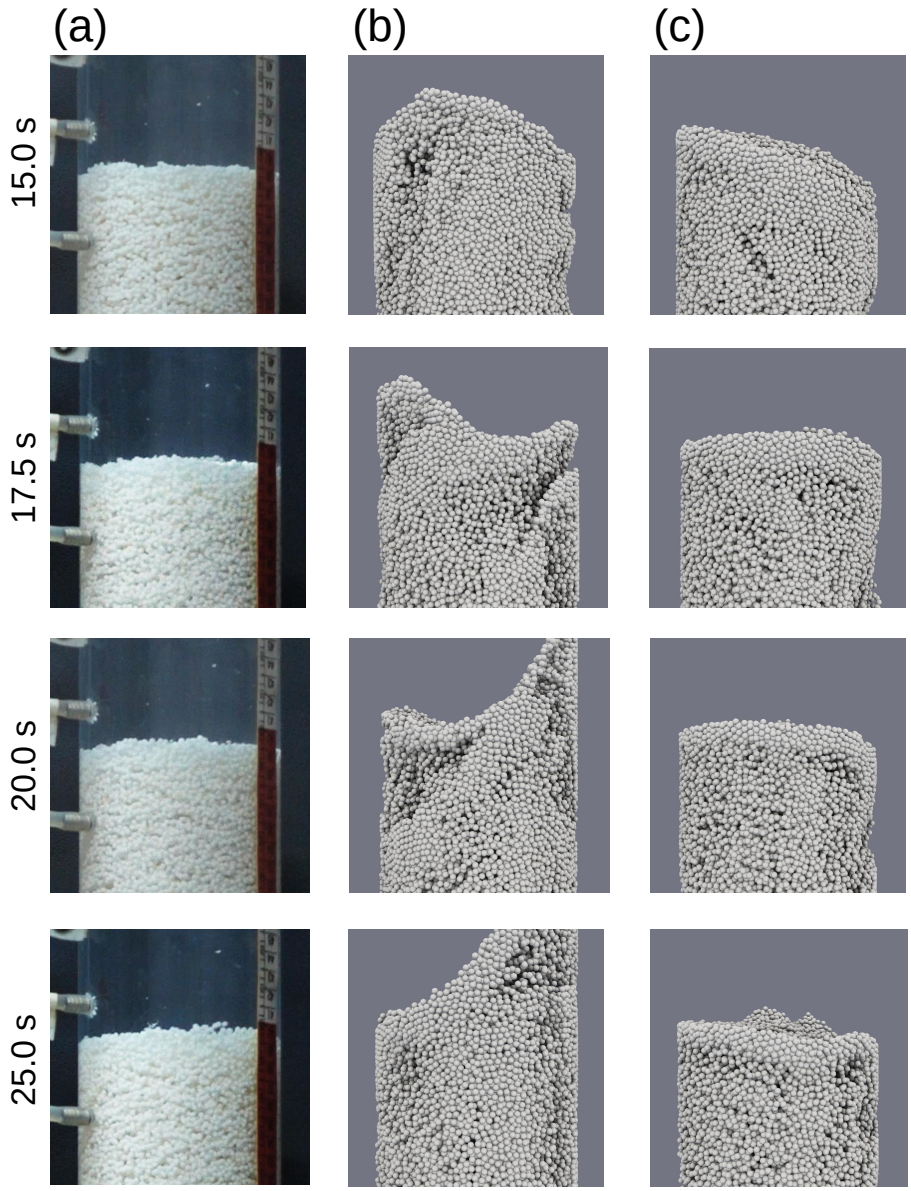

Figure 5: Images of the top of the pseudo-steady state (reached around 10 seconds of simulation)

alginate particles bed with 2.5 seconds intervals for (a) experimental, (b) simulation with drag force only, and (c) simulation with drag and lift forces results at the highest inlet velocity ($U/U_0 = 0.3595$).

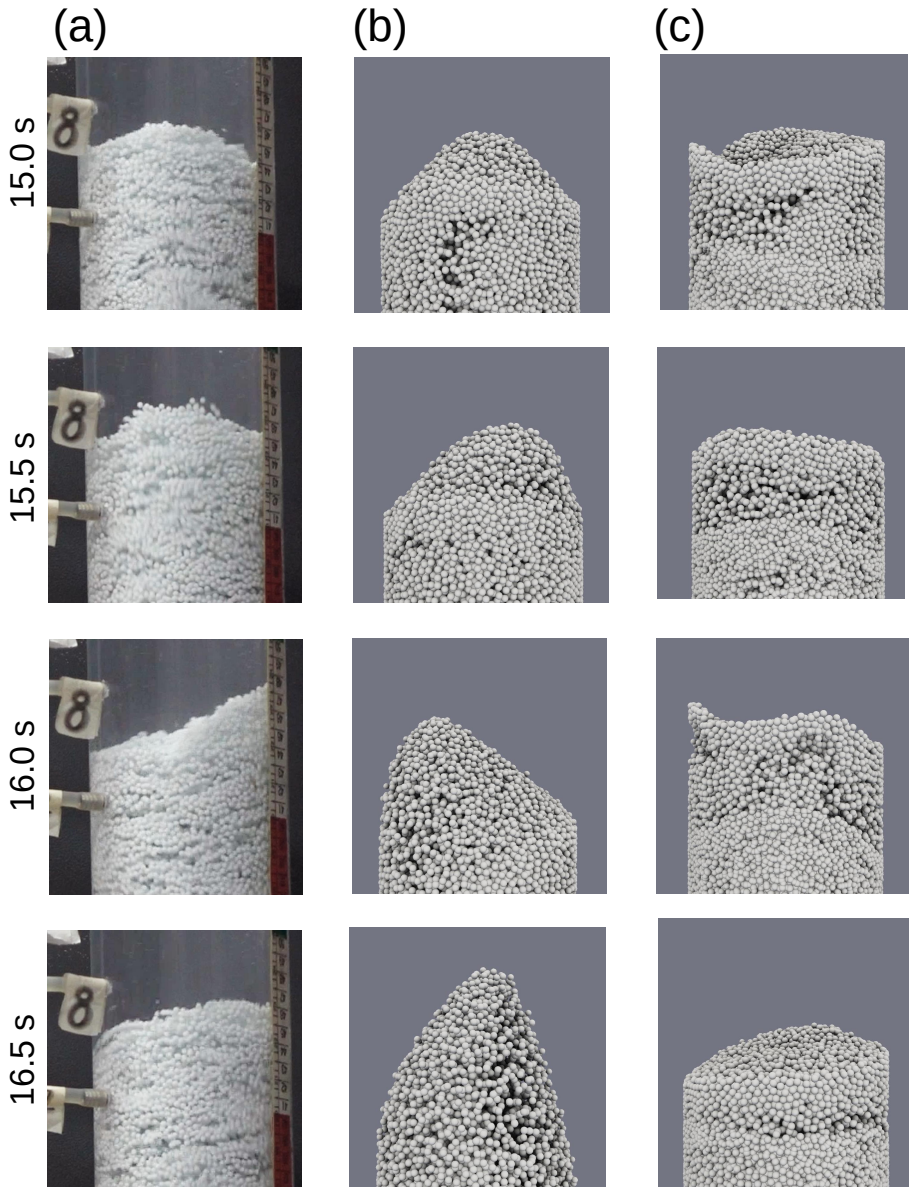

Figure 6: Images of the top of the pseudo-steady-state (reached around 4 seconds of simulation)

alumina particles bed with 0.5 seconds intervals for (a) experimental, (b) simulation with drag force only, and (c) simulation with drag and lift forces results at the highest inlet velocity ($U/U_0 = 0.3270$).

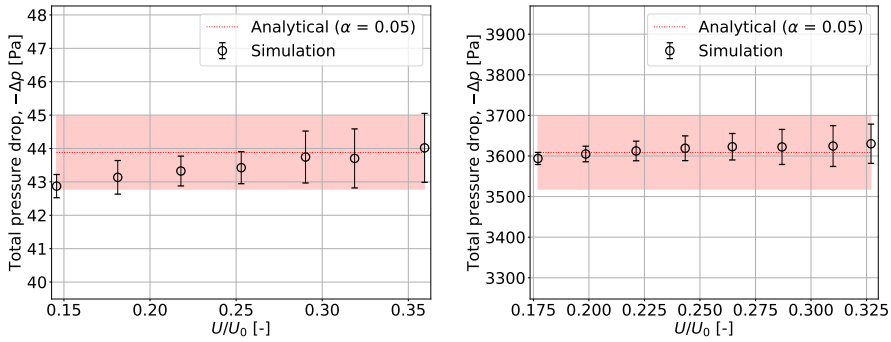

(a) Alginate (b) Alumina

Figure 7: Average of the total pressure difference for the (a) alginate and (b) alumina particles

the void fraction reduces the drag force sufficiently to prevent particles from fluidizing. Consequently, the equipment's bottom wall carries the weight of a few particles and this reduces the pressure drop. This effect can be observed in Figure 8.

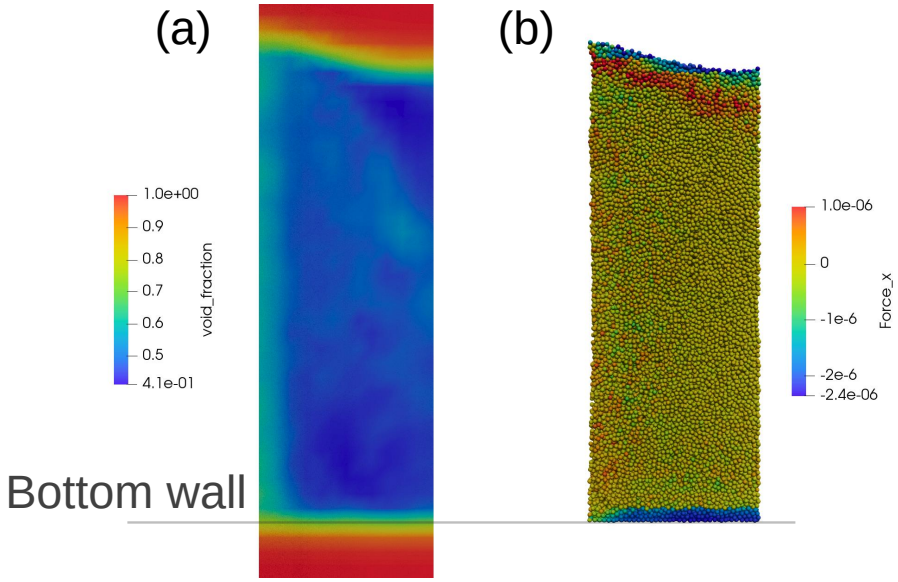

Figure 8: Snapshot of the $U/U_0 = 0.1430$ alginate particles simulation at 35 seconds (last time-step), showing (a) the void fraction profile and (b) the total force acting over particles in Newtons. Results are clipped in the axial direction to show the middle of the equipment. It can clearly be seen that the first few layers of particles are supported by the bottom wall.

The small fluctuations in the pressure are within realistic values. They are mainly related to the dynamics of the bed, which attests to numerical stabil-

ity throughout the simulations, especially considering all results collected inside the pseudo-stationary regime. Other authors found higher oscillations of pressure (e.g., 14) in the simulation of fluidized beds using Finite Volume codes. We usually expect higher variations when PCM is applied due to the coarse approximation of the void fraction field [18]. In this sense, since we are using PCM, the stability of the pressure field is attributed to void fraction smoothing, which improves the continuity of the field, and the grad-div stabilization, which enhances mass conservation [32].

5.2.2. Bed expansion

The bed expansion is usually represented by the spatial average of the void fraction along the bed's volume (or bed porosity) $\bar{\varepsilon_f}$. In the design of LSFB reactors, porosity is among the essential variables because of its use in predicting mass/heat transfer and conversion of reactants. Unlike gas-solids fluidized beds, it is well established that LSFBs tend to present a uniform porosity.

In Figure 9 we present the numerical and experimental results of the porosity measurement for both particles. We also present the results of the estimation of $\bar{\varepsilon_f}$ by the R-Z Equation (Equation 1), for comparison.

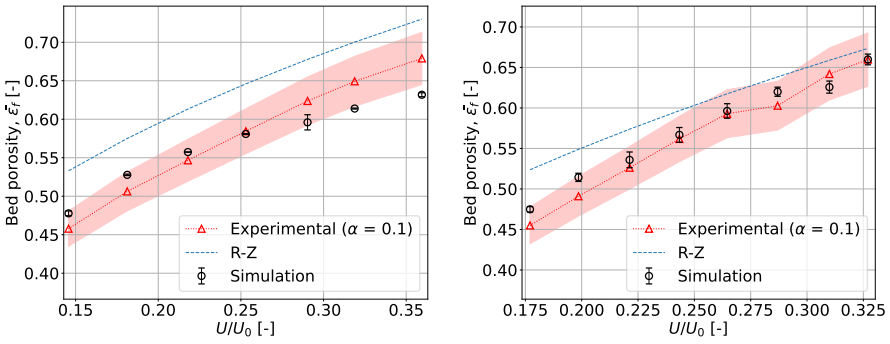

(a) Alginate

(b) Alumina

Figure 9: Bed porosity for (a) alginate and (b) alumina particles.

Almost all simulations fall into the experimental results region with a two-tail confidence interval of 90% ($\alpha = 0.1$). The agreement between simulations and experiment results is better assessed when comparing the results using R-Z. For the alginate, the RMSE is 78% higher than R-Z estimations (RMSE = 0.0618) compared to simulations (RMSE = 0.0347). The difference was even higher for alumina, reaching 168% (RMSE = 0.0417 for R-Z and 0.0156 for simulations). In the case of the alumina particles, the bed expansion was fully captured by the simulations, with all results staying within the confidence interval. The lower fitting in the case of the alginate particles can be associated with the diameter distribution of particles, which is not considered in the simulations. It is also important to note that, for all results, the bed expansion was stable with time, with a very low standard deviation (as noted in Figure 9).

These results highlight the reliability of unresolved CFD-DEM on the representation of particle-liquid fluidized beds. Furthermore, since the alginate particle's density is about a third of the alumina particles, it also reveals that the technique is reliable for a wide range of regimes, from the lowest fluid inlet velocity ($Re = 534$) to the highest ($Re = 19021$).

5.3. Mesh topology

As discussed by several authors (e.g., 18, 53, 54), the mesh resolution of the fluid representation is limited by the size of the particles. This is a limitation of the volume-averaging approach applied to this work, which is not mesh-independent. As a rule of thumb, when PCM is applied, $S_c/d_p > 3$ is recommended, which, in the case of coarse particles like the ones in this work, imposes an important limitation on the mesh. In the case of finer meshes, the mesh is too fine to have an accurate void fraction profile (even when smoothing is applied), affecting the precision of the drag force calculation. On the other hand, coarser meshes have an inadequate resolution to coherently capture the fluid dynamics.

One way to mitigate this limitation is to use a more continuous void fraction calculation method. In the present work, we did so by smoothing the void fraction field. Alternatives include computationally intensive analytical methods [55, 56] and more efficient but less precise non-analytical methods [57, 53]. In the context of the Finite Element Method, the Quadrature-Centered Method by Geitani and Blais [58], which is a computationally efficient analytical method for void fraction calculation, is a good alternative. It is worth mentioning that there are other Eulerian-Lagrangian alternatives to the unresolved CFD-DEM approach adopted in this work such as strategies that employ volume filtering [59] , two-grid formulation [60], and kernel-based approximation to the fluid field [54], which allow for particle-to-cell size ratios close to 1 but involve the implementation of more complex algorithms.

Although the mesh resolution independency test was not carried out, we assessed the sensitivity of the method to the mesh topology. As pointed out, one crucial reason for applying void fraction smoothing is to compensate for the mesh elements' size unequal distribution. To test whether a more uniform cell size distribution along the cylinder radius impacts the dynamics of the particles, we tested two other mesh topologies. These meshes are presented in Figure 10.

The difference between Mesh 1 (Figure 2) and 2 is that the length of the square side in Mesh 1 is way smaller, but the distribution of cells is the same. Mesh 3 is completely unstructured in the radial direction but has the same cell distribution as Meshes 1 and 2 along its height.

Besides the better distribution of cell sizes in Meshes 2 and 3, no changes in the overall behavior of the particles were observed when compared to Mesh 1. A slightly worse representation of the behavior of the particles is observed for the higher inlet flow rates using Mesh 2, even using the same smoothing strategy and applying the Saffman lift force. This can be attributed to its distortion in the outer cells, i.e., since the shape of the outer cells in Mesh 2 are irregular (sides do not present similar lengths), the void fraction profile in the radial direction (discussed in Section 5.1) is even more non-uniform. Since

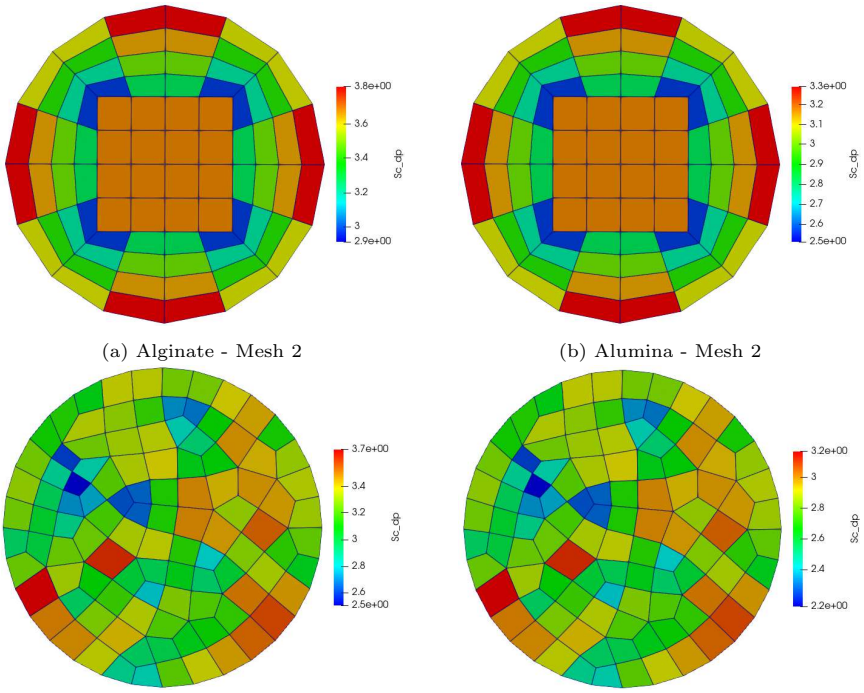

(a) Alginate - Mesh 2

(b) Alumina - Mesh 2

(c) Alginate - Mesh 3

(d) Alumina - Mesh 3

Figure 10: S_c/d_p for the different mesh and particle combinations.

drag is highly dependent of the void fraction, the plumbing effect represented in Figures 5 and 6 are even more prominent. However, Mesh 3 produced results similar to the original mesh presented in Figure 2 for all simulation conditions and particles.

In terms of quantitative analysis, the total pressure drop and bed expansion for all simulations with the different meshes stood close to one another. The quantitative results of the mesh test are presented in Figure 11.

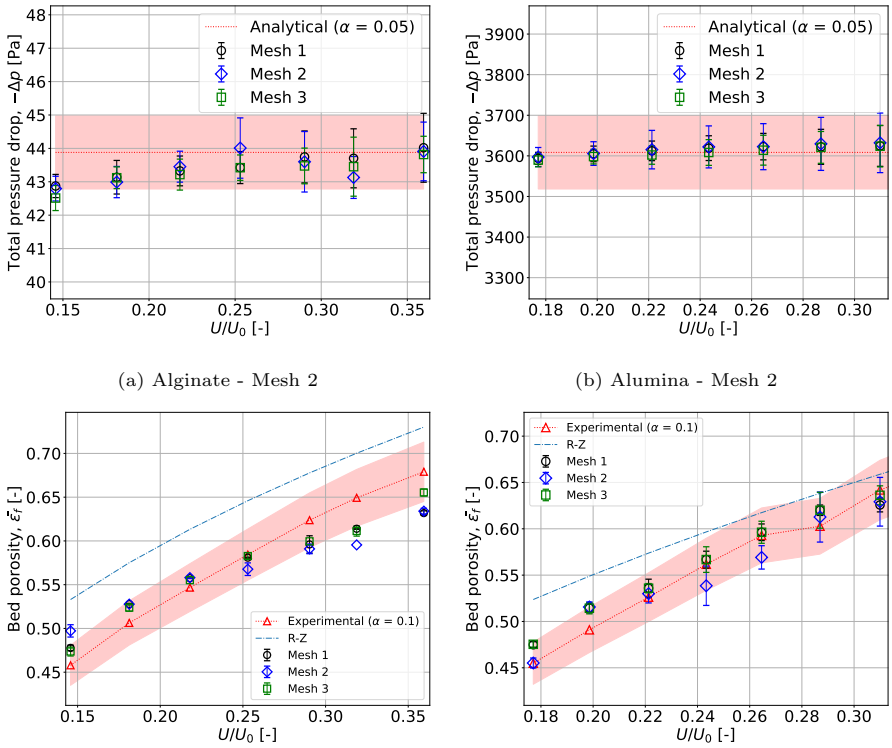

(a) Alginate - Mesh 2

(b) Alumina - Mesh 2

(c) Alginate - Mesh 3

(d) Alumina - Mesh 3

Figure 11: Bed expansion and pressure drop for the different mesh and particle combinations.

As observed in Figure 11, the quantitative results for all meshes and both particles present high similarity. Through the deviation, we observed slightly higher oscillations on the pressure field for Mesh 2 compared to the others, which can be attributed to the previously mentioned oscillatory behavior of the particles due to the distribution of mesh element sizes. Such oscillations lead to higher variability of the bed expansion in the tests with Mesh 2. Even so, the results stood within the experimental tolerance.

5.4. Drag model comparison

One way to assess the precision of drag correlations in representing liquid-solid fluidized beds is by evaluating its capability of reproducing the bed expansion according to the inlet velocity. The results in Figure 12 demonstrated that Rong, Di Felice, and Beetstra drag correlations precisely reproduce the observed behavior of the bed expansion as a function of the inlet velocity. Almost all points stood within the confidence interval, except for some alginate results. In the case of Beetstra, the highest distance between the simulated and experimental results is for the lowest inlet velocity (simulation 14% higher than experiment). It is important to note that the structure of the correlations is significantly different from one to another, especially considering Beetstra, so the results are reassuring from a validation point of view since they show that relatively accurate results can be obtained with unresolved CFD-DEM.

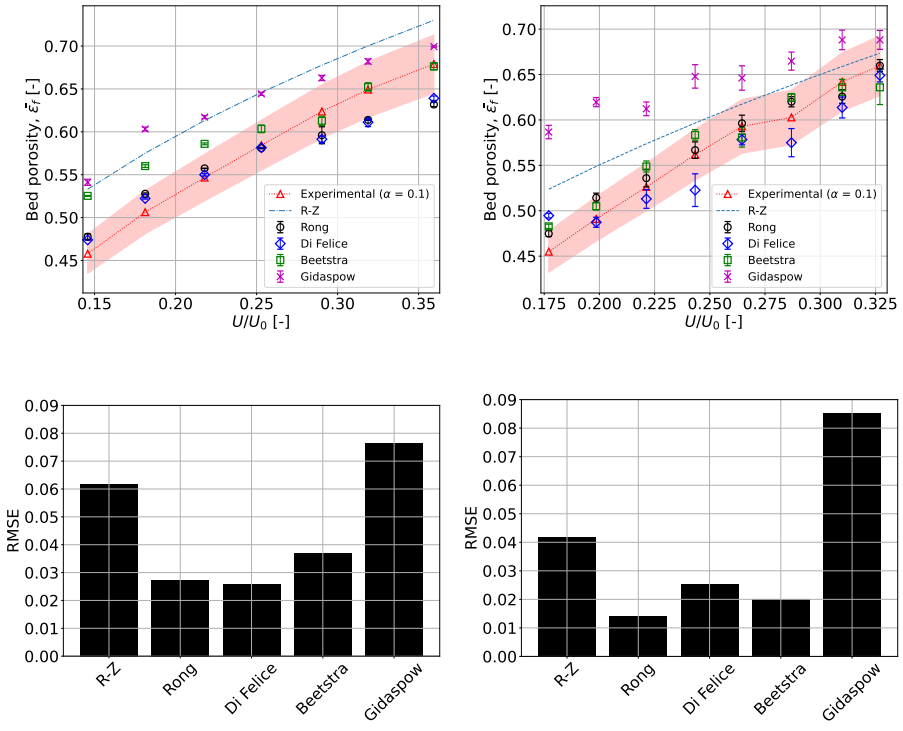

(a) Alginate

(b) Alumina

Figure 12: Bed porosity with different drag correlations for (a) alginate and (b) alumina particles.

According to several authors [39, 40, 41, 42, 37], neglecting ε_f in the exponent of $G(\varepsilon_f, \mathrm{Re}_{p,i})$ (Equation 27) can lead to important lack of accuracy. However, in the case of this work, the correlation proposed by Di Felice was the one with

the highest similarity with the alginate experimental results. Since all models are, in fact, correlations, i.e., come from fitting an equation to a given data, the lack of fitting with different data is expected. In the case of Rong and Beetstra drag correlations, since the models are highly complex, overfitting ε_f is a hypothesis for the slightly lower accuracy compared to Di Felice. Apart from that, all models could capture the experimental behavior of the bed.

Lack of fitting is found in Gidaspow drag correlation results. For both particles, the last points are the only ones within the 90% double tail confidence interval. The RMSE obtained using Gidaspow was 23% and 104% higher than the R-Z estimations for the alginate and alumina, respectively. The Gidaspow drag model is the only one that severely underperforms among the drag models tested.

In Figures 13 and 14, we compare the C_D calculated using all correlations in this work with C_D^{Rong} (calculated using the Rong drag model) for the alginate and alumina particles, respectively. This comparison is done by presenting a surface plot of C_D/C_D^{Rong} as a function of $\mathrm{Re}_p/\varepsilon_f$ and ε_f.

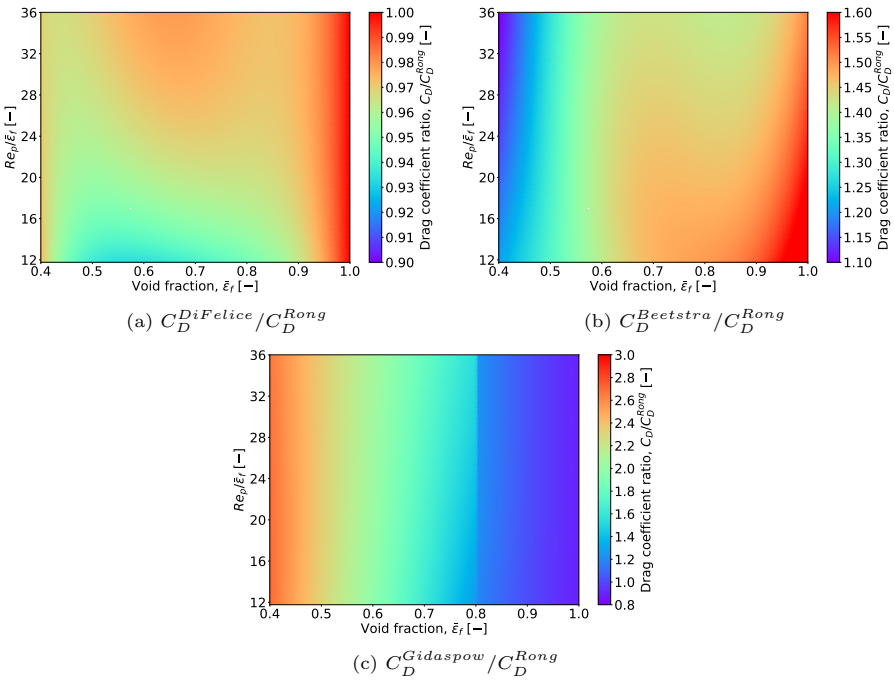

(a) $C_D^{DiFelice}/C_D^{Rong}$

(b) $C_D^{Beetstra}/C_D^{Rong}$

(c) $C_D^{Gidaspow}/C_D^{Rong}$

Figure 13: C_D/C_D^{Rong} comparison among correlations for the alginate particles, showing the ratios a) $C_D^{DiFelice}/C_D^{Rong}$, b) $C_D^{Beetstra}/C_D^{Rong}$, and c) $C_D^{Gidaspow}/C_D^{Rong}$ for Di Felice, Beetstra, and Gidaspow, respectively. Color scales are different for each correlation due to their high discrepancy.

As shown in Figures 13a and 14a, $C_D^{DiFelice}/C_D^{Rong}$ is very close to 1.0 in most of the studied region. For the alginate particles (Figure 13a), the drag coefficient

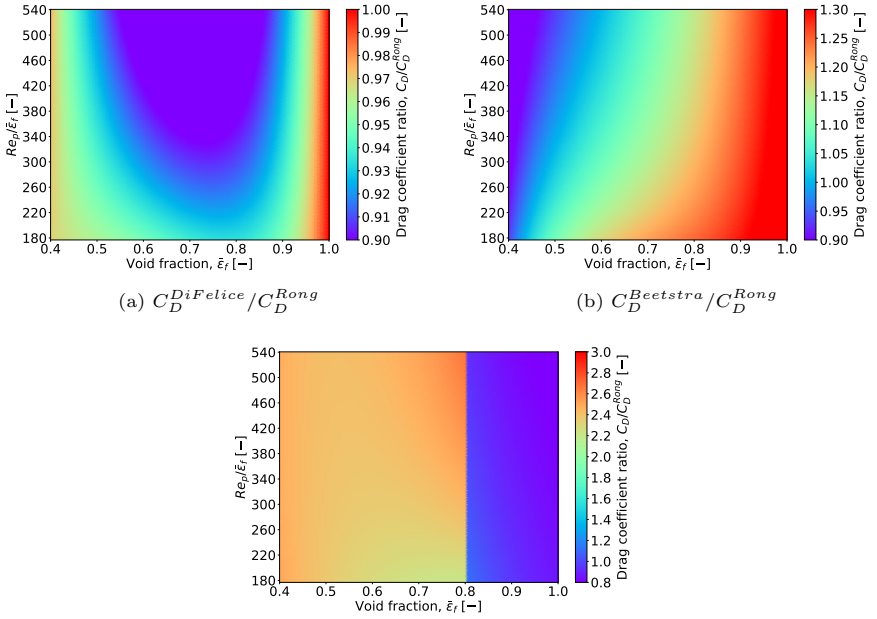

(a) $C_D^{DiFelice}/C_D^{Rong}$

(b) $C_D^{Beetstra}/C_D^{Rong}$

(c) $C_D^{Gidaspow}/C_D^{Rong}$

Figure 14: C_D/C_D^{Rong} comparison among correlations for the alumina particles, showing the ratios a) $C_D^{DiFelice}/C_D^{Rong}$, b) $C_D^{Beetstra}/C_D^{Rong}$, and c) $C_D^{Gidaspow}/C_D^{Rong}$ for Di Felice, Beetstra, and Gidaspow, respectively. Color scales are different for each correlation due to their high discrepancy.

is almost identical for most void fractions and particle Reynolds numbers, which explains the similarity between the results of both correlations in Figure 12a. As for the alumina particles, the center of the graphic in Figure 14a deviates from 1, which also has an effect on the porosity trend observed in Figure 12b.

$C_D^{Beetstra}/C_D^{Rong}$ (Figures 13a and 14a) highlights the higher sensitivity of Beetstra drag correlation to the flow regime. In the case of the alumina particles, the average $C_D^{Beetstra}/C_D^{Rong}$ for the studied region was 1.1, showing a considerably higher drag coefficient only at very dilute regions ($\varepsilon_f > 0.8$), and significantly lower at very concentrated regions with high Re_p; both rarely occurring in the case of fluidized beds. On the other hand, for alginate, the average ratio was 1.4, not reaching 1.0 in any region of the graphic, which explains the detachment between Rong and Beetstra in Figure 12a.

As for the Gidaspow drag correlation, $C_D^{Gidaspow}/C_D^{Rong}$ was, on average, 1.7 and 1.9 for alginate and alumina particles, respectively. The Gidaspow drag correlation is considerably less sensitive to ε_f, with a slightly better agreement with the experimental data at dilute regions, close to the limit when the model by Wen and Yu [35] takes place. However, the important discontinuity in this region can lead to highly unphysical drag force distribution in those regions. Similar features on $C_D^{Gidaspow}$ were observed by Marchelli et al. [61].

6. Conclusions

In the present work, we used Lethe [30, 17], a FEM-based CFD and DEM code with CFD-DEM coupling capabilities, to simulate the behavior of a pilot-scale liquid-solid fluidized bed. The numerical results were compared with experiments with water and for two distinct particle types: alginate ($\rho_p = 1029\mathrm{kg\,m^{-3}}$) and alumina ($\rho_p = 3586\mathrm{kg\,m^{-3}}$). We made all comparisons in the pseudo-steady-state regime for a considerable interval of real-time and multiple fluidization velocities.

Comparisons between simulations with and without Saffman lift force show that the application of the force creates more realistic dynamics of particles, avoiding channeling close to the walls caused by inherent distortions on the void fraction distribution along the radius. This result is in agreement with other results in the literature [10, 52, 24]

The comparison between experimental and simulated total pressure drop shows that the simulations could accurately represent the interphase momentum change of the real system for all the inlet conditions and both particles. Furthermore, this result shows that the magnitude of drag was successfully achieved.

Bed average porosity comparisons also show that the numerical results agree with the experiments in bed expansion. Bed porosities predicted by the simulations showed better agreement with experiments than the Richardson-Zaki equation [2] with the n index calculated by the correlation proposed by Khan and Richardson [3]. It is worth emphasizing the consistency of all tested conditions.

Tests with meshes with different topologies presented a high agreement with each other and the experiments. Higher unwanted oscillations in the dynamics of the particles are observed when the outer cell layers of the cylinder have a lower aspect ratio, which negatively impacts the void fraction radial distribution and drag. However, the quantitative results indicate a close fitting between experiments and simulations with all meshes.

Comparison between the drag correlations proposed by Rong et al. [37], Di Felice [36], Beetstra et al. [41], and Gidaspow [7] shows that the Di Felice, Rong, and Beetstra drag correlations are capable of reproducing the experimental behavior, presenting better precision on the reproduction of the experimental bed expansion than the Richardson-Zaki equation. The only exception was Gidaspow.

The results of the present work highlight the capability of the unresolved CFD-DEM to simulate a variety of solid-fluid systems in a wide range of flow regimes with high precision. Since the method is phenomenological, extrapolations of the case for other liquid-particle systems may be valid. However, additional work on solid-fluid force submodels is required to maximize the accuracy of this approach. We recommend the application of Saffman lift forces and void fraction smoothing liquid fluidized beds unresolved CFD-DEM simulations. Cells with high aspect ratios are also recommended to avoid the need for void fraction smoothing lengths larger than $2d_p$.

7. Acknowledgements

Thanks are due to São Paulo Research Foundation (FAPESP, grant #2019/19173-9, and grant #2020/14567-6); the Funding Authority for Studies and Projects of the Ministry of Science, Technology and Innovation (FINEP/MCTI) by means of the Program of Human Resources of the Brazilian National Petroleum Agency (PRH-ANP/MCTI); and the Brazilian National Council for Scientific and Technological Development (CNPq, process number 408618/2018-3) for financial support. The authors also thank Federal University of São Carlos (UFSCar) and Polytechnique Montréal for the infrastructure and all the technical support. This study was financed in part by the Coordenação de Aperfeicoamento de Pessoal de Nível Superior Brasil (CAPES) Finance Code 001.

We would like to acknowledge the financial support from the Natural Sciences and Engineering Research Council of Canada (NSERC) through the RGPIN-2020-04510 Discovery Grant. The authors would also like to acknowledge technical support and computing time provided by Compute Canada and Calcul Québec.

References

[1] Norman Epstein. Applications of Liquid-Solid Fluidization. *International Journal of Chemical Reactor Engineering*, 1(1), nov 2003. doi: 10.2202/1542-6580.1010.

[2] J.F. Richardson and W.N. Zaki. Sedimentation and fluidisation: Part i. *Chemical Engineering Research and Design*, 75:S82–S100, dec 1954. doi: 10.1016/s0263-8762(97)80006-8.

[3] A.R. Khan and J.F. Richardson. Fluid-particle interactions and flow characteristics of fluidized beds and settling suspensions of spherical particles. *Chemical Engineering Communications*, 78(1):111–130, apr 1989. doi: 10.1080/00986448908940189.

[4] S. Rapagn, R. Di Felice, L. G. Gibilaro, and P. U. Fuoscolo. Steady-state expansion characteristics of monosize spheres fluidised by liquids. *Chemical Engineering Communications*, 79(1):131–140, may 1989. doi: 10.1080/00986448908940031.

[5] Norman Epstein. *Handbook of fluidization and fluid-particle systems*. CRC Press, 2003. ISBN 0-8247-0259-X.

[6] T. B. Anderson and Roy Jackson. Fluid Mechanical Description of Fluidized Beds. Equations of Motion. *Industrial & Engineering Chemistry Fundamentals*, 6(4):527–539, nov 1967. doi: 10.1021/i160024a007.

[7] Dimitri Gidaspow. *Multiphase Flow and Fluidization: Continuum and Kinetic Theory Descriptions*. Academic Press, Boston, 1994. ISBN 9780122824708.

[8] Jack T. Cornelissen, Fariborz Taghipour, Renaud Escudié, Naoko Ellis, and John R. Grace. CFD modelling of a liquid–solid fluidized bed. *Chemical Engineering Science*, 62(22):6334–6348, nov 2007. doi: 10.1016/j.ces.2007.07.014.

[9] Rupesh K. Reddy and Jyeshtharaj B. Joshi. CFD modeling of solid–liquid fluidized beds of mono and binary particle mixtures. *Chemical Engineering Science*, 64(16):3641–3658, aug 2009. doi: 10.1016/j.ces.2009.05.004.

[10] Daniela M. Koerich, Gabriela C. Lopes, and Leonardo M. Rosa. Investigation of phases interactions and modification of drag models for liquid-solid fluidized bed tapered bioreactors. *Powder Technology*, 339:90–101, nov 2018. doi: 10.1016/j.powtec.2018.07.102.

[11] Patrícia Metolina and Gabriela Cantarelli Lopes. Numerical analysis of liquid-solid flow in tapered and cylindrical fluidized beds for wastewater treatment and biogas production. *Energy Conversion and Management*, 187:447–458, may 2019. doi: 10.1016/j.enconman.2019.02.092.

[12] Md. Tariqul Islam and Anh V. Nguyen. Effect of particle size and shape on liquid–solid fluidization in a HydroFloat cell. *Powder Technology*, 379:560–575, feb 2021. doi: 10.1016/j.powtec.2020.10.080.

[13] Z. Y. Zhou, S. B. Kuang, K. W. Chu, and A. B. Yu. Discrete particle simulation of particle–fluid flow: model formulations and their applicability. *Journal of Fluid Mechanics*, 661:482–510, aug 2010. doi: 10.1017/s002211201000306x.

[14] Bruno Blais, Manon Lassaigne, Christoph Goniva, Louis Fradette, and François Bertrand. Development of an unresolved CFD–DEM model for the flow of viscous suspensions and its application to solid–liquid mixing. *Journal of Computational Physics*, 318:201–221, aug 2016. doi: 10.1016/j.jcp.2016.05.008.

[15] Ariane Bérard, Gregory S. Patience, and Bruno Blais. Experimental methods in chemical engineering: Unresolved CFD-DEM. *The Canadian Journal of Chemical Engineering*, 98(2):424–440, jan 2020. doi: 10.1002/cjce.23686.

[16] H.P. Zhu, Z.Y. Zhou, R.Y. Yang, and A.B. Yu. Discrete particle simulation of particulate systems: Theoretical developments. *Chemical Engineering Science*, 62(13):3378–3396, jul 2007. doi: 10.1016/j.ces.2006.12.089.

[17] Shahab Golshan, Peter Munch, Rene Gassmller, Martin Kronbichler, and Bruno Blais. Lethe-DEM: an open-source parallel discrete element solver with load balancing. *Computational Particle Mechanics*, 10(1):77–96, may 2022. doi: 10.1007/s40571-022-00478-6.

[18] Zhengbiao Peng, Elham Doroodchi, Caimao Luo, and Behdad Moghtaderi. Influence of void fraction calculation on fidelity of CFD-DEM simulation of gas-solid bubbling fluidized beds. *AIChE Journal*, 60(6):2000–2018, mar 2014. doi: 10.1002/aic.14421.

[19] A Di Renzo and Francesco Paolo Di Maio. Homogeneous and bubbling fluidization regimes in DEM–CFD simulations: Hydrodynamic stability of gas and liquid fluidized beds. *Chemical Engineering Science*, 62(1-2):116–130, jan 2007. doi: 10.1016/j.ces.2006.08.009.

[20] Alberto Di Renzo, Fernando Cello, and Francesco Paolo Di Maio. Simulation of the layer inversion phenomenon in binary liquid–fluidized beds by DEM–CFD with a drag law for polydisperse systems. *Chemical Engineering Science*, 66(13):2945–2958, jul 2011. doi: 10.1016/j.ces.2011.03.035.

[21] Bruno Blais, Olivier Bertrand, Louis Fradette, and François Bertrand. CFD-DEM simulations of early turbulent solid–liquid mixing: Prediction of suspension curve and just-suspended speed. *Chemical Engineering Research and Design*, 123:388–406, jul 2017. doi: 10.1016/j.cherd.2017.05.021.

[22] Bruno Blais and François Bertrand. CFD-DEM investigation of viscous solid–liquid mixing: Impact of particle properties and mixer characteristics. *Chemical Engineering Research and Design*, 118:270–285, feb 2017. doi: 10.1016/j.cherd.2016.12.018.

[23] Mauricio Maestri, Gabriel Salierno, Stella Piovano, Miryan Cassanello, María Angélica Cardona, Daniel Hojman, and Héctor Somacal. CFD-DEM modeling of solid motion in a water-calcium alginate fluidized column and its comparison with results from radioactive particle tracking. *Chemical Engineering Journal*, 377:120339, dec 2019. doi: 10.1016/j.cej.2018.11.037.

[24] Tim M.J. Nijssen, Hans A.M. Kuipers, Jan van der Stel, Allert T. Adema, and Kay A. Buist. Complete liquid-solid momentum coupling for unresolved CFD-DEM simulations. *International Journal of Multiphase Flow*, 132: 103425, nov 2020. doi: 10.1016/j.ijmultiphaseflow.2020.103425.

[25] Joo P. F. Campos, Karla R. B. Melo, and Gabriela C. Lopes. Implementation, validation and application of a lubrication force model in CFD-DEM simulations. *Brazilian Journal of Chemical Engineering*, 39(2):429–440, jul 2021. doi: 10.1007/s43153-021-00134-1.

[26] Julia Picabea, Mauricio Maestri, Miryan Cassanello, Gabriel Salierno, Cataldo De Blasio, María Angélica Cardona, Daniel Hojman, and Héctor Somacal. Validation of CFD-DEM simulation of a liquid–solid fluidized bed by dynamic analysis of time series. *Particuology*, 68:75–87, sep 2022. doi: 10.1016/j.partic.2021.11.003.

[27] Li Liang and Efstathios E. Michaelides. The magnitude of basset forces in unsteady multiphase flow computations. *Journal of Fluids Engineering*, 114(3):417–419, sep 1992. doi: 10.1115/1.2910047.

[28] A. Hager, C. Kloss, S. Pirker, and C. Goniva. Parallel resolved open source CFD-DEM: Method, validation and application. *The Journal of Computational Multiphase Flows*, 6(1):13–27, mar 2014. doi: 10.1260/1757-482x.6.1.13.

[29] Bruno Blais, David Vidal, Francois Bertrand, Gregory S. Patience, and Jamal Chaouki. Experimental methods in chemical engineering: Discrete element method—DEM. *The Canadian Journal of Chemical Engineering*, 97(7):1964–1973, jun 2019. doi: 10.1002/cjce.23501.

[30] Bruno Blais, Lucka Barbeau, Valérie Bibeau, Simon Gauvin, Toni El Geitani, Shahab Golshan, Rajeshwari Kamble, Ghazaleh Mirakhori, and Jamal Chaouki. Lethe: An open-source parallel high-order adaptative CFD solver for incompressible flows. *SoftwareX*, 12:100579, jul 2020. doi: 10.1016/j.softx.2020.100579.

[31] Toni El Geitani, Shahab Golshan, and Bruno Blais. Towards High-Order CFD-DEM: Development and Validation. *Industrial &amp Engineering Chemistry Research*, jan 2023. doi: 10.1021/acs.iecr.2c03546.

[32] Toni El Geitani, Shahab Golshan, and Bruno Blais. A high-order stabilized solver for the volume averaged Navier-Stokes equations. *International Journal for Numerical Methods in Fluids*, feb 2023. doi: 10.1002/fld.5182.

[33] P. A. Cundall and O. D. L. Strack. A discrete numerical model for granular assemblies. *Géotechnique*, 29(1):47–65, mar 1979. doi: 10.1680/geot.1979.29.1.47.

[34] Sabri Ergun. Fluid flow through packed columns. *Chemical Engineering Progress*, 48(2):89–94, 1952.

[35] C. Wen and Y. Yu. Mechanics of fluidization. In *Chemical Engineering Progress Symposium Series*, 1966.

[36] R. Di Felice. The voidage function for fluid-particle interaction systems. *International Journal of Multiphase Flow*, 20(1):153–159, feb 1994. doi: 10.1016/0301-9322(94)90011-6.

[37] L.W. Rong, K.J. Dong, and A.B. Yu. Lattice-Boltzmann simulation of fluid flow through packed beds of uniform spheres: Effect of porosity. *Chemical Engineering Science*, 99:44–58, August 2013. doi: 10.1016/j.ces.2013.05.036.

[38] Joseph Marius DallaValle. *Micromeritics: The Technology of Fine Particles*. Pitman Pub. Corp., 2 edition, 1948.

[39] Sofiane Benyahia, Madhava Syamlal, and Thomas J. O'Brien. Extension of hill-koch-ladd drag correlation over all ranges of reynolds number and solids volume fraction. *Powder Technology*, 162(2):166–174, mar 2006. doi: 10.1016/j.powtec.2005.12.014.

[40] Luca Mazzei and Paola Lettieri. A drag force closure for uniformly dispersed fluidized suspensions. *Chemical Engineering Science*, 62(22):6129–6142, nov 2007. doi: 10.1016/j.ces.2007.06.028.

[41] R. Beetstra, M. A. van der Hoef, and J. A. M. Kuipers. Drag force of intermediate reynolds number flow past mono- and bidisperse arrays of spheres. *AIChE Journal*, 53(2):489–501, 2007. doi: 10.1002/aic.11065.

[42] Fernando Cello, Alberto Di Renzo, and Francesco Paolo Di Maio. A semi-empirical model for the drag force and fluid–particle interaction in polydisperse suspensions. *Chemical Engineering Science*, 65(10):3128–3139, may 2010. doi: 10.1016/j.ces.2010.02.006.

[43] Clayton T. Crowe, John D. Schwarzkopf, Martin Sommerfeld, and Yutaka Tsuji. *Multiphase Flows with Droplets and Particles*. CRC Press, aug 2011. doi: 10.1201/b11103.

[44] P. G. Saffman. The lift on a small sphere in a slow shear flow. *Journal of Fluid Mechanics*, 22(2):385–400, jun 1965. doi: 10.1017/s0022112065000824.

[45] P. G. Saffman. The lift on a small sphere in a slow shear flow - corrigendum. *Journal of Fluid Mechanics*, 31(3):624–624, feb 1968. doi: 10.1017/s0022112068999990.

[46] R. Mei. An approximate expression for the shear lift force on a spherical particle at finite reynolds number. *International Journal of Multiphase Flow*, 18(1):145–147, jan 1992. doi: 10.1016/0301-9322(92)90012-6.

[47] Gabriela C. Lopes, Xiatao Bi, Norman Epstein, Susan A. Baldwin, and John R. Grace. Hydrodynamic characteristics of particles with different roughness and deformability in a liquid fluidized bed. *Chemical Engineering Science*, 185:50–63, aug 2018. doi: 10.1016/j.ces.2018.03.058.

[48] Karla R. B. Melo, John R. Grace, and Gabriela C. Lopes. A new correlation for the coefficient of restitution of particles with low mechanical resistance for modeling wastewater treatment biofilm reactors. *Clean Technologies and Environmental Policy*, 24(2):623–632, apr 2021. doi: 10.1007/s10098-021-02079-y.

[49] G. Bradski. The opencv library. *Dr. Dobb's Journal of Software Tools*, 2000.

[50] W. Christian D. Brown, R. Hanson. Tracker video analysis and modeling tool. 2022.

[51] L. Prieto Saavedra, C. E. N. Radburn, A. Collard-Daigneault, and B. Blais. An implicit large-eddy simulation perspective on the flow over periodic hills. *arXiv preprint arXiv:2206.08145v1*, 2022. doi: 10.48550/ARXIV.2206.08145.

[52] Hussein Zbib, Mohammadreza Ebrahimi, Farhad Ein-Mozaffari, and Ali Lohi. Comprehensive analysis of fluid-particle and particle-particle interactions in a liquid-solid fluidized bed via CFD-DEM coupling and tomography. *Powder Technology*, 340:116–130, dec 2018. doi: 10.1016/j.powtec.2018.09.009.

[53] Daniel A. Clarke, Andrew J. Sederman, Lynn F. Gladden, and Daniel J. Holland. Investigation of Void fraction Schemes for Use with CFD-DEM Simulations of Fluidized Beds. *Industrial & Engineering Chemistry Research*, 57(8):3002–3013, feb 2018. doi: 10.1021/acs.iecr.7b04638.

[54] Zekun Wang, Yujun Teng, and Moubin Liu. A semi-resolved CFD–DEM approach for particulate flows with kernel based approximation and hilbert curve based searching strategy. *Journal of Computational Physics*, 384:151–169, may 2019. doi: 10.1016/j.jcp.2019.01.017.

[55] C.L. Wu, J.M. Zhan, Y.S. Li, K.S. Lam, and A.S. Berrouk. Accurate void fraction calculation for three-dimensional discrete particle model on unstructured mesh. *Chemical Engineering Science*, 64(6):1260–1266, mar 2009. doi: 10.1016/j.ces.2008.11.014.

[56] Ben Freireich, Madhusudhan Kodam, and Carl Wassgren. An exact method for determining local solid fractions in discrete element method simulations. *AIChE Journal*, 56(12):3036–3048, nov 2010. doi: 10.1002/aic.12223.

[57] H. A. Khawaja, S. A. Scott, M. S. Virk, and M. Moatamedi. Quantitative analysis of accuracy of voidage computations in CFD-DEM simulations. *The Journal of Computational Multiphase Flows*, 4(2):183–192, jun 2012. doi: 10.1260/1757-482x.4.2.183.

[58] Toni El Geitani and Bruno Blais. Quadrature-Centered Averaging Scheme for Accurate and Continuous Void Fraction Calculation in Computational Fluid Dynamics–Discrete Element Method Simulations. *Industrial &amp Engineering Chemistry Research*, mar 2023. doi: 10.1021/acs.iecr.3c00172.

[59] Jesse Capecelatro and Olivier Desjardins. An euler–lagrange strategy for simulating particle-laden flows. *Journal of Computational Physics*, 238: 1–31, apr 2013. doi: 10.1016/j.jcp.2012.12.015.

[60] Surya Deb and Danesh K. Tafti. A novel two-grid formulation for fluid–particle systems using the discrete element method. *Powder Technology*, 246:601–616, sep 2013. doi: 10.1016/j.powtec.2013.06.014.

[61] Filippo Marchelli, Qinfu Hou, Barbara Bosio, Elisabetta Arato, and Aibing Yu. Comparison of different drag models in CFD-DEM simulations of spouted beds. *Powder Technology*, 360:1253–1270, jan 2020. doi: 10.1016/j.powtec.2019.10.058.